The effect of long timescale gas dynamics on femtosecond filamentation

Y.-H. Cheng, J. K. Wahlstrand, N. Jhajj, and H. M. Milchberg*

Institute for Research in Electronics and Applied Physics, University of Maryland, College Park, Maryland 20742, USA

*milch@umd.edu

Abstract: Femtosecond laser pulses filamenting in various gases are shown to generate long- lived quasi-stationary cylindrical depressions or 'holes' in the gas density. For our experimental conditions, these holes range up to several hundred microns in diameter with gas density depressions up to ~20%. The holes decay by thermal diffusion on millisecond timescales. We show that high repetition rate filamentation and supercontinuum generation can be strongly affected by these holes, which should also affect all other experiments employing intense high repetition rate laser pulses interacting with gases.

©2013 Optical Society of America

OCIS codes: (190.5530) Pulse propagation and temporal solitons; (350.6830) Thermal lensing; (320.6629) Supercontinuum generation; (260.5950) Self-focusing.

References and Links

1. A. Couairon and A. Mysyrowicz, "Femtosecond filamentation in transparent media," Phys. Rep. **441**(2-4), 47–189 (2007).
2. P. B. Corkum, C. Rolland, and T. Srinivasan-Rao, "Supercontinuum generation in gases," Phys. Rev. Lett. **57**(18), 2268–2271 (1986).
   S. A. Trushin, K. Kosma, W. Fuss, and W. E. Schmid, "Sub-10-fs supercontinuum radiation generated by filamentation of few-cycle 800 nm pulses in argon," Opt. Lett. **32**(16), 2432–2434 (2007).
3. N. Zhavoronkov, "Efficient spectral conversion and temporal compression of femtosecond pulses in SF_6," Opt. Lett. **36**(4), 529–531 (2011).
4. C. P. Hauri, R. B. Lopez-Martens, C. I. Blaga, K. D. Schultz, J. Cryan, R. Chirla, P. Colosimo, G. Doumy, A. M. March, C. Roedig, E. Sistrunk, J. Tate, J. Wheeler, L. F. Dimauro, and E. P. Power, "Intense self-compressed, self-phase-stabilized few-cycle pulses at 2 microm from an optical filament," Opt. Lett. **32**(7), 868–870 (2007).
   C. P. Hauri, W. Kornelis, F. W. Helbing, A. Heinrich, A. Couairon, A. Mysyrowicz, J. Biegert, and U. Keller, "Generation of intense, carrier-envelope phase-locked few-cycle laser pulses through filamentation," Appl. Phys. B **79**(6), 673–677 (2004).
5. G. Stibenz, N. Zhavoronkov, and G. Steinmeyer, "Self-compression of millijoule pulses to 7.8 fs duration in a white-light filament," Opt. Lett. **31**(2), 274–276 (2006).
6. F. Vidal, D. Comtois, C.-Y. Chien, A. Desparois, B. La Fontaine, T. W. Johnston, J.-C. Kieffer, H. P. Mercure, H. Pepin, and F. A. Rizk, "Modeling the triggering of streamers in air by ultrashort laser pulses," IEEE Trans. Plasma Sci. **28**(2), 418–433 (2000).
7. S. Tzortzakis, B. Prade, M. Franco, A. Mysyrowicz, S. Hüller, and P. Mora, "Femtosecond laser-guided electric discharge in air," Phys. Rev. E Stat. Nonlin. Soft Matter Phys. **64**(5), 057401 (2001).
8. J. P. Palastro, T. M. Antonsen, Jr., and H. M. Milchberg, "Compression, spectral broadening, and collimation in multiple, femtosecond pulse filamentation in atmosphere," Phys. Rev. A **86**(3), 033834 (2012).
9. T. R. Clark and H. M. Milchberg, "Time- and space-resolved density evolution of the plasma waveguide," Phys. Rev. Lett. **78**(12), 2373–2376 (1997).
10. T. R. Clark and H. M. Milchberg, "Time-evolution and guiding regimes of the laser-produced plasma waveguide," Phys. Plasmas **7**(5), 2192–2197 (2000).
11. Y.-H. Chen, S. Varma, A. York, and H. M. Milchberg, "Single-shot, space- and time-resolved measurement of rotational wavepacket revivals in H_2, D_2, N_2, O_2, and N_2O," Opt. Express **15**(18), 11341–11357 (2007).
12. J. K. Wahlstrand, Y.-H. Cheng, Y.-H. Chen, and H. M. Milchberg, "Optical nonlinearity in Ar and N_2 near the ionization threshold," Phys. Rev. Lett. **107**(10), 103901 (2011).
13. S. Tzortzakis, B. Prade, M. Franco, and A. Mysyrowicz, "Time-evolution of the plasma channel at the trail of a self-guided IR femtosecond laser pulse in air," Opt. Commun. **181**(1-3), 123–127 (2000).

J. K. Wahlstrand, Y.-H. Chen, Y.-H. Cheng, S. R. Varma, and H. M. Milchberg, "Measurements of the high field optical nonlinearity and electron density in gases: application to filamentation experiments," IEEE J. Quantum Electron. **48**(6), 760–767 (2012).

14. K. P. Birch, "Precise determination of refractometric parameters for atmospheric gases," J. Opt. Soc. Am. A **8**(4), 647–651 (1991).

15. M. D. Feit and J. A. Fleck, Jr., "Light propagation in graded-index optical fibers," Appl. Opt. **17**(24), 3990–3998 (1978).

K. Y. Kim, I. Alexeev, and H. M. Milchberg, "Single-shot measurement of laser-induced double step ionization of helium," Opt. Express **10**(26), 1563–1572 (2002).

16. Y.-H. Chen, S. Varma, T. M. Antonsen, and H. M. Milchberg, "Direct measurement of the electron density of extended femtosecond laser pulse-induced filaments," Phys. Rev. Lett. **105**(21), 215005 (2010).

17. C. I. Blaga, F. Catoire, P. Colosimo, G. G. Paulus, H. G. Muller, P. Agostini, and L. F. DiMauro, "Strong-field photoionization revisited," Nat. Phys. **5**(5), 335–338 (2009).

18. http://webbook.nist.gov/chemistry/fluid/

W. M. Haynes, Handbook of Chemistry and Physics, 93rd edition (CRC Press, 2012), http://www.hbcpnetbase.com/

19. D. V. Kartashov, A. V. Kirsanov, A. M. Kiselev, A. N. Stepanov, N. N. Bochkarev, Y. N. Ponomarev, and B. A. Tikhomirov, "Nonlinear absorption of intense femtosecond laser radiation in air," Opt. Express **14**(17), 7552–7558 (2006).

20. J. K. Wahlstrand, Y.-H. Cheng, and H. M. Milchberg, "Absolute measurement of the transient optical nonlinearity in N_2, O_2, N_2O, and Ar," Phys. Rev. A **85**(4), 043820 (2012).

21. S. Varma, Y.-H. Chen, J. P. Palastro, A. B. Fallahkair, E. W. Rosenthal, T. Antonsen, and H. M. Milchberg, "Molecular quantum wake-induced pulse shaping and extension of femtosecond air filaments," Phys. Rev. A **86**(2), 023850 (2012).

1. Introduction

Filamentation of femtosecond laser pulses in gases is an area of wide and increasing interest owing to applications such as harmonic generation, supercontinuum generation, and the possibility of generating greatly extended plasma conducting channels [1]. Filaments are produced by the interplay between self-focusing induced by the bound electron nonlinearity in the atoms or molecules of the gas and defocusing from the plasma generated by the self-focused laser light. Typically, millijoule-level optical laser pulses are sufficient for extended filaments. A common application of filaments is broad frequency spectrum generation and pulse shortening [2–5] in sealed gas cells, where the laser driver is a high pulse repetition rate system, which can typically range up to 5 kHz.

In this paper, we demonstrate that femtosecond filaments can generate long-lived, radially localized and axially extended depressions in the gas density that gradually dissipate via thermal diffusion on a millisecond timescale. The effect is significant even with pulse energies as low as ~100 µJ. At sufficiently high laser pump repetition rates, we find that the long timescale gas dynamics can strongly influence the propagation of pulses in the pulse train. The drop in gas density caused by heating from nonlinear absorption of the laser is thought to play a role at the <100 ns timescale in the triggering of electrical discharges by filaments [6,7], but to our knowledge the very long time scale behavior has not been recognized to affect filamentation at high pulse repetition rates.

The experiment consists of three parts. In the first part, we demonstrate the effect of laser pulse repetition rate on the self-focusing collapse and filament spectrum as a function of propagation distance in room air. In the second part, we examine the effect of pulse repetition rate on supercontinuum generation in a Xenon gas cell. In the third part, we present results of longitudinal interferometry measurements of long timescale gas evolution after femtosecond laser interaction. We then present simulations of the density hole evolution and use those results to gain physical insight and interpret our experiments.

2. Experiments

For all experiments, the laser pulses were generated by a 1 kHz Ti:Sapphire laser system capable of producing up to 3.5 mJ, 40 fs pulses centered at 800 nm. For the air filament experiment we used 0.9-1.5 mJ laser pulses focused at f/600 with a 3 m lens. The filament core spectrum was measured as a function of propagation distance by scanning a rail-mounted

pinhole along the propagation path and collecting the forward emission on the exit side. The pinhole was prepared prior to the experiment by drilling a ~300 μm diameter hole in a thin Teflon sheet with the 1 kHz filamenting beam at multiple axial locations. This guaranteed negligible further pinhole erosion during a full axial scan. The filament was generated on an enclosed optical table to minimize shot-to-shot transverse position movement from air currents in the laboratory. The filament propagation terminates within ~2 mm past the pinhole exit. Simulations using the propagation code of ref [8]. show that no additional nonlinear frequency broadening is imparted beyond this point. Therefore, the collected spectrum is that of the propagating laser at the filament core. For this experiment, the laser was operated at 1 kHz but the repetition rate for focused pulses was controlled with chopper wheels synchronized to the laser timing. We found earlier that controlling the repetition rate with the laser's regenerative amplifier Pockels cell resulted in slight thermally-induced changes to the beam intensity profile and phase front which were sufficient to affect the filamentation collapse location.
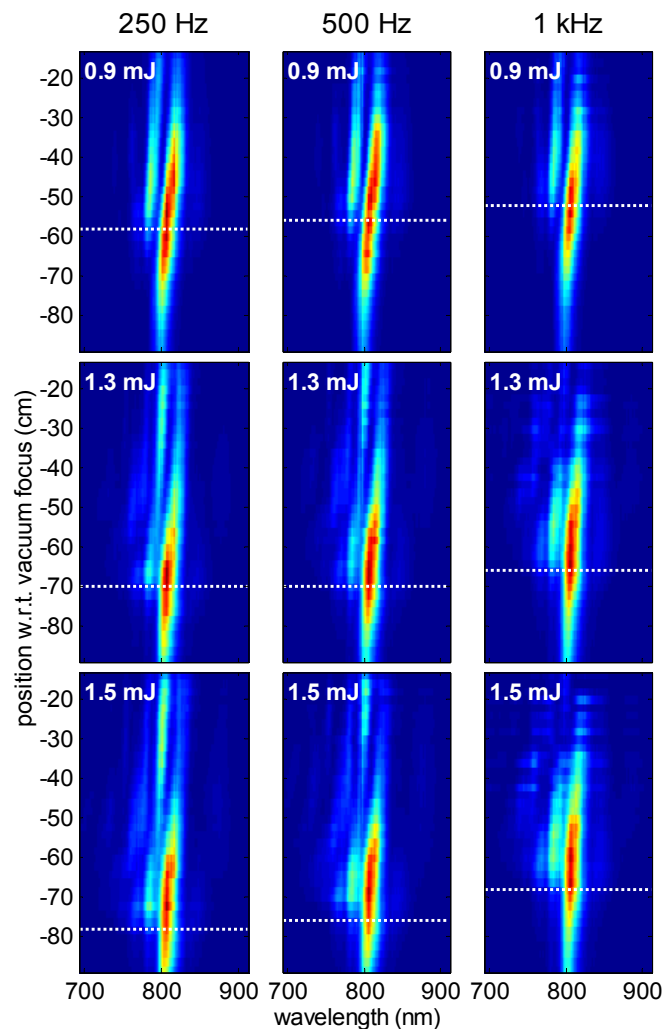

Fig. 1. Filament core spectrum vs. propagation distance as a function of pump energy and repetition rate. Propagation distance is measured with respect to the vacuum focus. The laser pulse propagates from below in these panels. The white dotted line shows the position of beam collapse to a filament.

The filament core spectrum as a function of axial position for three laser repetition rates and pulse energies is shown in Fig. 1. The laser pulse propagates from below. In each panel, the axial location of beam collapse to a filament is shown with a dotted line. This was observed by recording the axial location where plasma fluorescence begins and is coincident with the onset of a strong blue shift owing to gas ionization. It is seen that the collapse position moves farther from the lens as the pulse repetition rate increases from 250 Hz to 1 kHz, and this axial shift increases with pulse energy. The onset of spectral blue wings, the signature of plasma generation, follows this axial shift, and the extent of the blue wings increases with repetition rate, especially for the higher energy pulses.

We next investigated a very common arrangement in many labs that use high repetition rate lasers (typically 1 kHz) to generate supercontinuum spectra for compression or other applications [2–5]. Here, we focused 140-250 µJ pulses at f/100 into a gas cell filled with 2.2 atm Xenon, and examined the repetition rate-dependence of supercontinuum generation. The cell windows were sufficiently far from the beam waist that they contributed negligibly to the generated spectrum. The results are shown in Fig. 2. A normal incidence 800 nm dielectric mirror was used to filter the pump from the spectrum. It is seen that in all cases, the bluer parts of the spectra are dominant for the highest repetition rates, with the effect strongest at 140 µJ pump energy. The blue wing augmentation is even stronger than in the air filament case of Fig. 1.
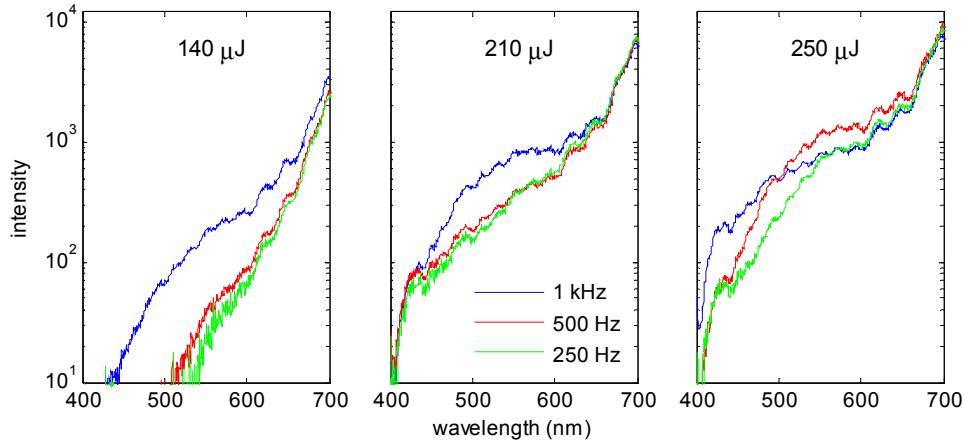

Fig. 2. Supercontinuum spectra vs. laser pulse energy and repetition rate.

To understand the origin of these repetition rate dependent effects, we performed longitudinal interferometry on femtosecond filament-excited gas. For this experiment, we operated the pump laser at 20 Hz (50 ms between pulses) in order to measure the long timescale gas dynamics driven by a single pump pulse. Since the results from the filament and supercontinuum experiments (Figs. 1 and 2) indicate possible dependence on a gas evolution timescale ranging up to milliseconds, we could not use a standard optical pump-probe delay line. Instead, we used a gated CCD camera and a continuous probe beam from a 635 nm CW diode laser which counter-propagated through the pump-excited interaction region, overlapping the pump beam. The setup is shown in Fig. 3.

The probe passed back through the pump focusing lens, was separated from the pump beam with a 800 nm dielectric mirror (M), and then was sent through a folded wavefront interferometer [9,10]. The vacuum focal plane of the pump laser beam was imaged onto a CCD camera at the exit of the interferometer. Temporal gating of the probe was obtained by triggering the CCD camera's electronic shutter with an adjustable delay with respect to the pump pulse. We used the minimum temporal window of the electronic shutter of ~40 µs,

which set the time resolution. As will be seen, this resolution is sufficient for measuring the long timescale gas response to the femtosecond pump pulse.
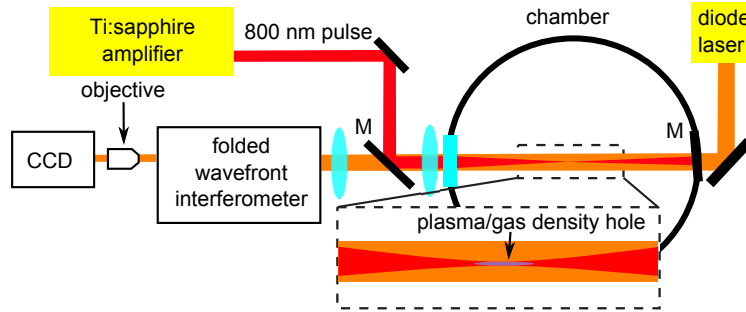

Fig. 3. Interferometry setup. The CW diode probe laser counter-propagates with respect to the pump beam direction, passes through the pump focusing lens, and enters the folded wavefront interferometer.
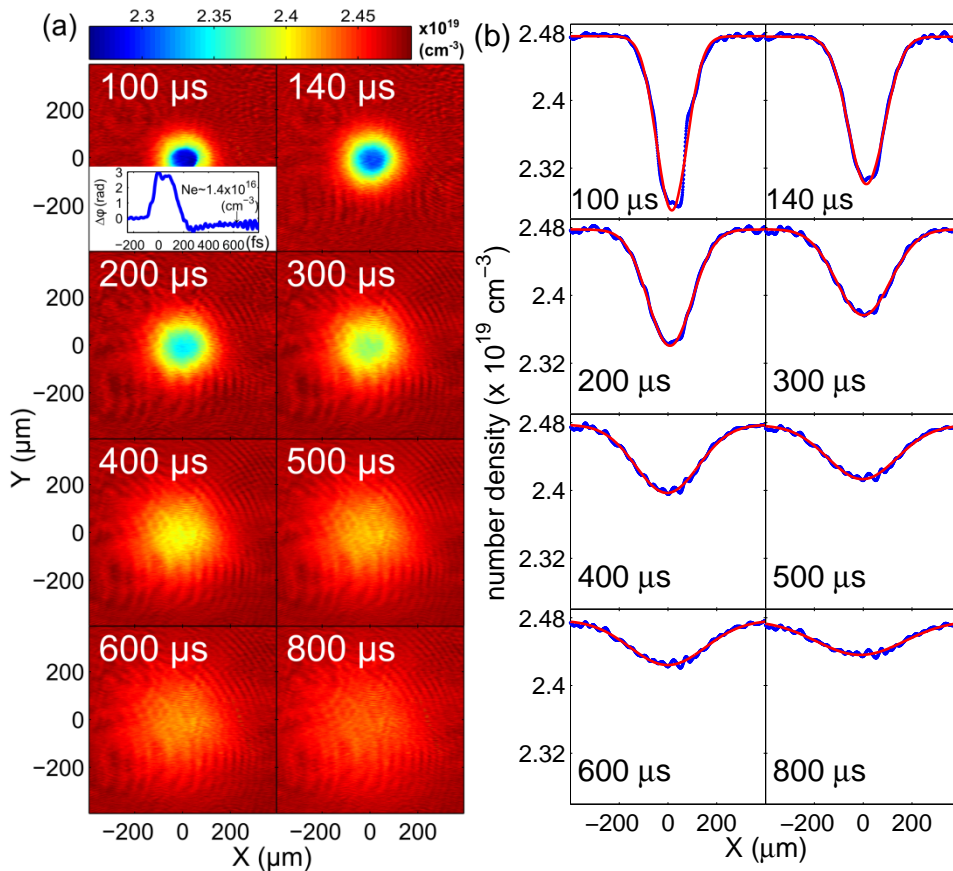

Fig. 4. (a) Gas average number density profiles vs. probe delay with respect to interaction of a 800 nm, 0.72 mJ, 40 fs pulse focused at f/65 into air at 1 atm. The inset shows electron density measured with spectral interferometry [11, 12]. (b) Lineouts of the air density profiles of Fig. 4(a). The blue curve is the measurement; the red curve is a Gaussian fit. The spatial resolution of the interferometric images is 10 μm. Density was extracted from phase shift maps using the linear polarizabilities of N_2 and O_2, $\beta_{N2} = 1.76 \times 10^{-24}$ cm^3 and $\beta_{O2} = 1.60 \times 10^{-24}$ cm^3 [14].

The linearly polarized 40 fs pump pulse was focused at f/65 into the chamber backfilled with various pressures of Kr, O_2, N_2, Ar, and air. The laser spot full width at half maximum (FWHM) diameter was ~60 μm. The pulse energy was adjusted using a waveplate and polarizer. Figure 4(a) shows, for pump energy 0.72 mJ, a sequence of gas density profiles in 1 atm air extracted from the interferograms using well-known fringe analysis techniques [10]. The inset in the upper left of the figure shows the time-dependent phase shift imposed on a collinear spectral interferometry probe in a temporal window centered on the pump (our spectral interferometry diagnostic is described in references [11,12]). The initial electron density of ~1.4×10^{16} cm^{-3} is extracted from the phase shift ~0.6 ps after the pump pulse.

By the first frame shown in the sequence, at 40 μs delay after the pump, the plasma has long ceased to exist, as it will have recombined well before ~10 ns [13]. The 2D gas density profile is an average over the CW probe laser's interaction length. The density profile is extracted from the 2D phase shift profile, the known linear polarizabilities of nitrogen and oxygen [14] and an interaction length of ~18 mm, determined by the axial extent of the filament's plasma fluorescence. Simulations of the probe beam propagation using the BPM method [15] show negligible refractive phase front distortion that could complicate interpretation of our 2D phase extraction.
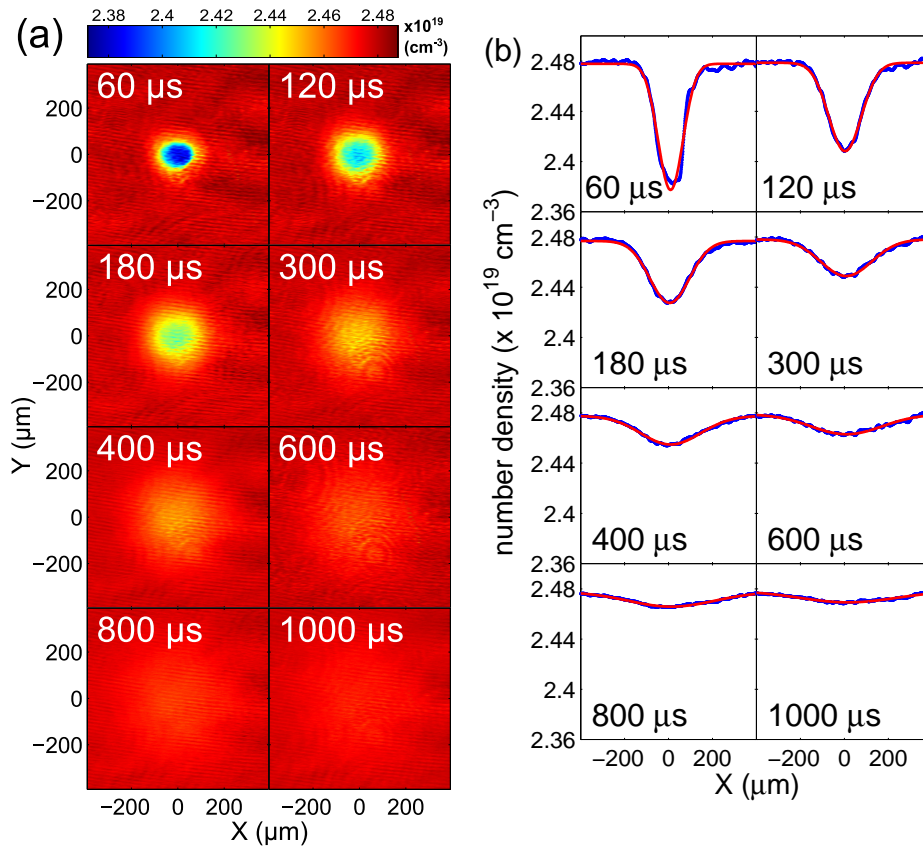

Fig. 5. (a) Number density profiles vs. probe delay with respect to interaction of a 800 nm, 0.72 mJ, 40 fs pulse focused at f/65 into N_2 at 1 atm. (b) Lineouts of the N_2 density profiles of Fig. 5(a). The blue curve is the measurement; the red curve is a Gaussian fit. The spatial resolution of the interferometric images is 10 μm. Density was extracted from phase shift maps using the linear polarizability of N_2, $\beta_{N2} = 1.76 \times 10^{-24}$ cm^3 [14].

Corresponding lineouts of the gas density are shown in Fig. 4(b), with Gaussian fit curves overlaying the data curves. The profile sequence shows the gas density hole widening and becoming shallower. By ~0.5 ms, there is only a ~1% density depression remaining. Figures 5(a) and (b) show similar plots for 1 atm of N_2. Qualitatively similar results occur for the other gases and pressures used.

3. Simulations of gas density hole evolution

To gain an understanding of the density hole evolution on gas type, pressure, and pump laser parameters, we performed simulations of the gas hydrodynamic evolution in cylindrical geometry using a one-dimensional Lagrangian one-fluid hydrocode, in which the conservation equations for mass, momentum and energy, $\partial \xi_i / \partial t + \nabla \cdot (\xi_i \mathbf{v} + \phi_i) = S_i$, were solved numerically. The mass equation has $\xi_1 = \rho$ and $\phi_1 = 0$, the momentum equation has $\xi_2 = \rho \mathbf{v}$ and $\phi_2 = P \vec{\mathbf{I}}$ (where $\vec{\mathbf{I}}$ is the unit tensor), and the energy equation has $\xi_3 = \varepsilon + \frac{1}{2} \rho \mathbf{v}^2$ and $\phi_3 = P\mathbf{v} + \mathbf{q}$. Here, ξ is the volume density of the conserved quantity, ϕ is the flux of that quantity, and S refers to sources or sinks, while ρ is mass density, ε is fluid internal energy density, $\mathbf{v}$ is fluid velocity, P is gas pressure, and $\mathbf{q}$ is the heat flux. At all times, $S_1 = S_2 = 0$ owing to mass and momentum conservation, but $S_3 \neq 0$ because the thermal part of the energy density is changed by laser heating and by ionization/recombination of all the relevant species in the gas. Solving the full set of fluid plus species population equations from the femtosecond through millisecond timescales requires accurate microscopic rates, including those for inelastic collisions, ionization, attachment, and recombination from the initial plasma at ~5 eV down to room temperature. Many of these rates are not well known. Furthermore, in principle one must keep track of all the species involved (atoms, ions, molecules, molecular ions) and their various states of excitation.

We can, however, proceed by recognizing that at times >>10 ns after laser excitation, all of the energy initially stored in free electron thermal energy and in the ionization and excitation distribution has been repartitioned into an essentially fully recombined gas in its ground electronic state. If the gas is molecular, for the conditions of our experiments it will also be in the ground vibrational state and in a thermal distribution of rotational states. Because the thermal conductivity of neutral gas is much smaller than that of plasma, the total energy initially deposited by the femtosecond laser pulse remains contained within a diameter comparable to the original laser spot size. As the ambipolar diffusion during the recombination process is much less than the laser spot width of ~50 μm, the 'initial' radial pressure distribution driving the gas hydrodynamics at times >10 ns is set by the initial plasma conditions $P_0(r) = N(r) k_B T(r) \approx (f_e / f_g) N_e(r) k_B T_e(r)$, where k_B is Boltzmann's constant, $N_e(r)$ and $T_e(r)$ are the initial electron density and electron temperature profiles immediately after femtosecond laser pumping of the gas, and $N(r)$ and $T(r)$ are the neutral gas number density and temperature profiles. This expression depends on the thermodynamic degrees of freedom of the free electrons ($f_e = 3$ translational degrees of freedom) and the gas, f_g, which depends on the gas type and temperature. In addition, an initial radial velocity profile with a weak positive gradient is imposed to mimic the results of our full hydrodynamic simulations at times <10 ns. In practice, our long timescale simulation results are insensitive to the detailed shapes of either the initial pressure profile or the fluid velocity profile, and depend mostly on the peak initial electron density and temperature and the radial scale length. To simulate the neutral gas response at long timescales we solve the fluid equations for the ξ_i, using $S_3 = 0$ and the initial pressure profile given by $P_0(r)$ above. We expect the fluid velocity field to relax over a timescale $\tau_{relax} \sim R_0 / c_s$, where R_0 is the initial radial scale of the laser heating, given by the laser spot radius, and $c_s = (k_B T / m)^{1/2}$ is the gas sound speed, where m is the atom or molecule mass. For $R_0 \sim 50$ μm, $N_e \sim 1.5 \times 10^{16}$ cm^{-3} and $k_B T_e \sim 5$ eV (typical filament electron density and temperature (see below)), and $N \sim 2.5 \times 10^{19}$

cm^{-3} for a 1 atm ambient gas, we find $\Delta T \sim 100$ K as a result of repartitioning and $\tau_{\text{relax}} \sim 1$ μs. As we shall see, this timescale is borne out by the fluid simulations: for all gases and pressures of this experiment, by a few microseconds after the laser interaction, the fluid velocity field has relaxed and the pressure becomes constant with radial position. A quasi-equilibrium is reached where the gas density profile is then just the inverse of the temperature profile, and further evolution is described by thermal diffusion.

To understand the earlier time evolution of the gas before the thermal diffusion-dominated phase, Fig. 6 shows simulation results in 1 atm N_2 capturing the dynamics at times <10 μs after the pump pulse. We used $N_e = 1.5 \times 10^{16}$ cm^{-3} and $k_B T_e = 5$ eV as the initial plasma conditions as the source of thermal energy repartitioned into the atmospheric pressure neutral gas. While there are direct measurements of filament electron density (see Fig. 4(a) and ref [16].), we rely on measurements of <10 eV electron spectra [17] from above threshold ionization in dilute nitrogen gas for laser intensity <10^{14} W/cm^2. As will be seen, the good agreement between measurements and simulations of the gas density hole justify this choice of initial electron temperature. The repartitioning of the plasma energy to neutral gas assumes 3 degrees of translational freedom of the molecules $\left(3 \times \frac{1}{2} k_B T\right)$ plus 2 degrees of rotational freedom $\left(2 \times \frac{1}{2} k_B T\right)$, so that $f_g = 5$. The resulting gas temperature change ($\Delta T \sim 100$ K) is insufficient for excitation of significant molecular vibration. It is seen that by ~1 μs, a sound wave has separated away from the interaction region and propagates to the simulation (absorbing) boundary, and by ~2 μs, a quasi-stationary density hole is established, in agreement with our earlier estimate for this timescale.
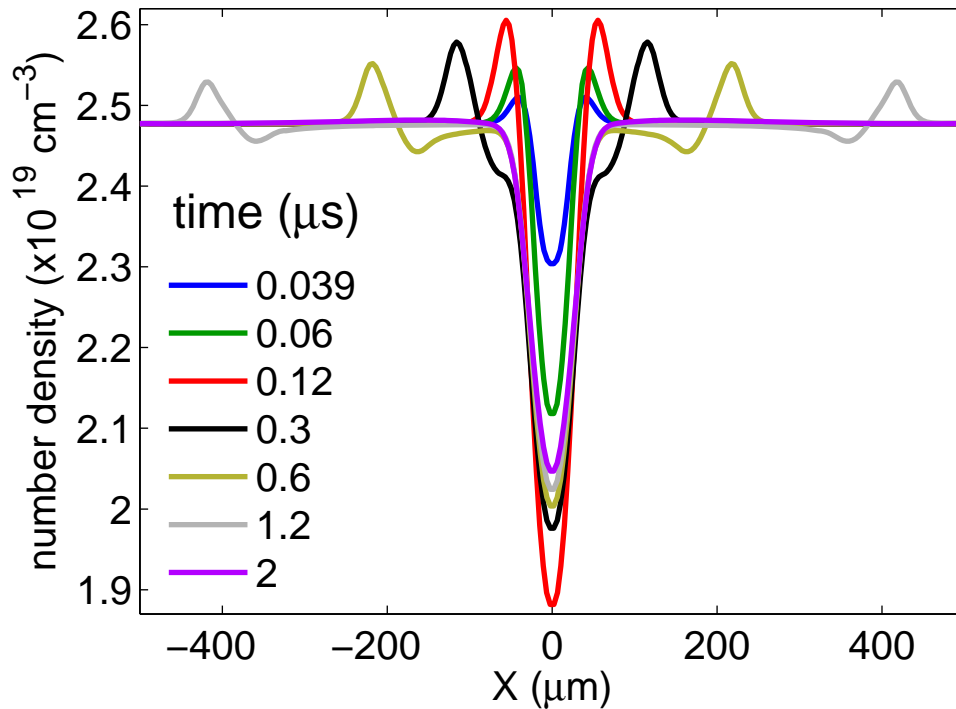

Fig. 6. Hydrodynamic simulation of the early phase of gas evolution of 1 atm N_2. Initial conditions are $N_e = 1.5 \times 10^{16}$ cm^{-3} and $k_B T_e = 5$ eV. The density profile becomes quasi-stationary by ~2 μs.
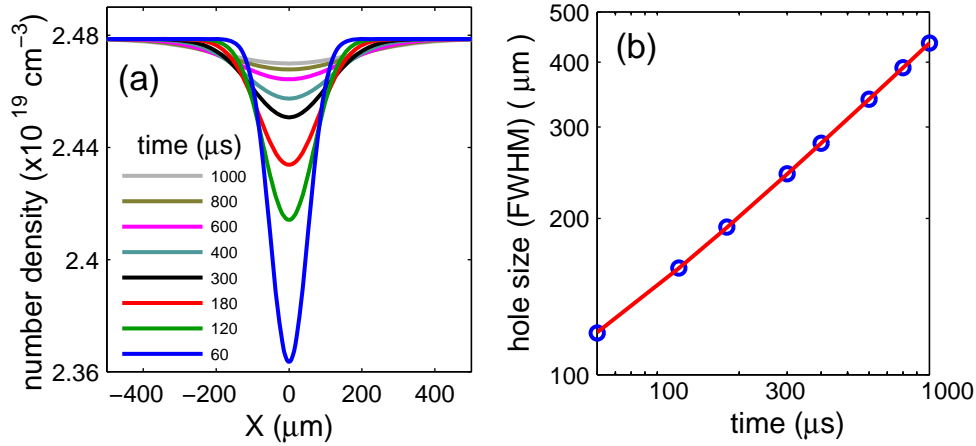
Fig. 7. (a) Simulated evolution of the gas density hole at later times. (b) Hole FWHM $d_{1/2}$ vs. time. The red curve is a fit to $d_{1/2} = \left(R_0^2 + 4\alpha t \right)^{1/2}$, indicating that the long time evolution of the gas is thermal diffusion dominated.

Figure 7(a) shows simulation results for times up to 1 ms for the same conditions as in Fig. 6. Good agreement is seen with the experimental N_2 density profiles of Fig. 5. In Fig. 7(b), we plot the hole FWHM diameter $d_{1/2}$ as a function of time. At these long times, the gas density profile evolution is governed completely by thermal diffusion, as indicated by the time dependence $d_{1/2} \sim t^{1/2}$. When there is no longer hydrodynamic motion ($\mathbf{v} \sim 0$), which is the case here after several microseconds as seen in Fig. 6, the energy conservation equation $\partial \xi_3 / \partial t + \nabla \cdot \left(\xi_3 \mathbf{v} + \phi_3 \right) = 0$ becomes $\partial \varepsilon / \partial t = -\nabla \cdot \mathbf{q}$. Using $\mathbf{q} = -\kappa \nabla T$, where κ is the neutral gas thermal conductivity, this becomes $\partial T / \partial t = \alpha \nabla^2 T$, the thermal diffusion equation, where $\alpha = \kappa / c_p$, assuming constant κ and specific heat capacity c_p. At the pressures used in our experiments, the gas dynamics are nearly ideal [18] with $c_p = 5Nk_B/2$ for a monatomic gas and $c_p = 7Nk_B/2$ for a gas of diatomic molecules. In the temperature range achieved after repartitioning of the initial plasma energy to the neutral gas ($\Delta T \sim 100$ K), the thermal conduction is only very weakly dependent on temperature. For an initial Gaussian temperature distribution with a $1/e$ radius of R_0, the solution to the thermal diffusion equation is $T(r,t) = T_0 \left(R_0^2 / \left(R_0^2 + 4\alpha t \right) \right) \exp\left(-r^2 / \left(R_0^2 + 4\alpha t \right) \right) + T_b$, where T_0 is the peak temperature and T_b is the background temperature (room temperature) of the gas. Because for our conditions the hydrodynamics has ceased after ~1 μs, the gas conforms to the pressure balance $N(r,t)T(r,t) = N_b T_b$, where N_b is the background gas density. For a relatively shallow depression, we get $\Delta N(r,t) = N_b T_0 T_b^{-1} \left(R_0^2 / \left(R_0^2 + 4\alpha t \right) \right) \exp\left(-r^2 / \left(R_0^2 + 4\alpha t \right) \right)$ for the density profile, where the width varies as $\sim \left(R_0^2 + 4\alpha t \right)^{1/2}$ and the depth varies as $\sim \left(R_0^2 + 4\alpha t \right)^{-1}$, with the holes in heavier gases (smaller κ and α) expanding and decaying more slowly. For $t > R_0^2 / 4\alpha$ (~10 μs for $R_0 = 50$ μm and 1 atm air), the width and depth vary as $\sim \left(\alpha t \right)^{1/2}$ and $\sim \left(\alpha t \right)^{-1}$. We note that the measured long timescale density profiles for all gases investigated are very well fit by Gaussians, of which Figs. 4(b) and 5(b) are examples.
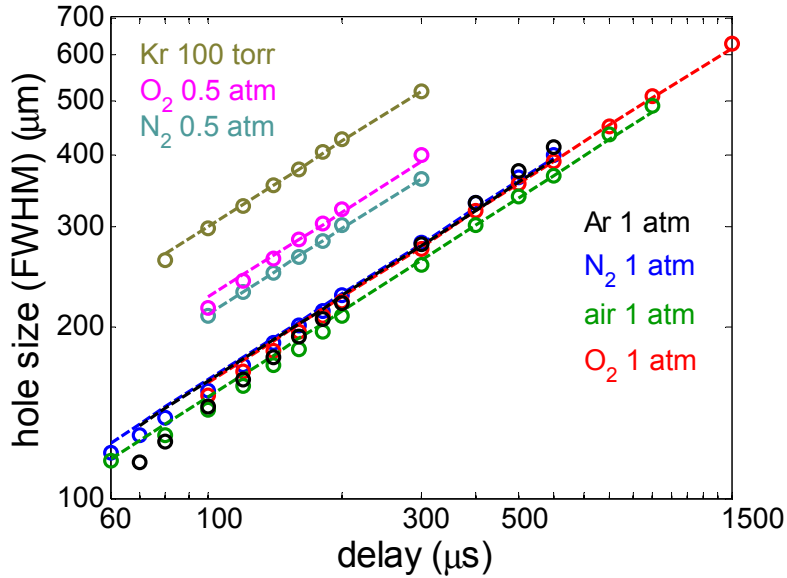
Fig. 8. Log-log plot of measured FWHM of density hole vs. time for our range of gases and conditions. The good fit to lines of slope ½ verifies that the long time gas evolution is dominated by thermal diffusion.

The fact that thermal diffusion dominates the long timescale evolution of all of our tested gases is highlighted by Fig. 8, which is a log-log plot of measured density hole FWHM diameter vs. time for a range of gases and pressures. All points are well fitted to lines with slope ½ as predicted by the thermal diffusion equation. The fitted lines were used to extract the thermal diffusion coefficients α of the gases, from which the thermal conductivities were determined by $\kappa = \alpha c_p$. These are compared to the literature values in Table 1, showing good agreement.

Table 1. Thermal Conductivities Extracted from Fits in Fig. 8 and Comparison to Literature Values

gas & pressure (T = 300K)	thermal conductivity κ (10^{-3}W/(m·K))	
	Extracted from $\kappa = \alpha c_p$	κ from literature [18]
N₂ 1 atm	28.3	25.60
O₂ 1 atm	27.9	26.35
air 1 atm	24.6	26.38
N₂ 0.5 atm	24.0	25.59
O₂ 0.5 atm	27.7	26.34
Kr 100 torr	9.1	9.28
Ar 1 atm	19.9	17.52

4. Discussion and conclusions

The effect of the long timescale gas density hole left by a pulse or sequence of pulses is to reduce the index of refraction near the center of the beam seen by the next pulse in the sequence. This will have a defocusing effect on the pulse. While the density profiles shown in Figs. 4 and 5 are induced by single pulses (a pump repetition rate of 20 Hz allows the density hole to completely relax between pulses), the density holes relevant to Figs. 1 and 2 have been cumulatively generated by the pulse train. Figure 9(a) shows a sequence of 2D density profiles for pump energy of 0.7 mJ at a repetition rate of 1 kHz in air at 1 atm. At all probe

delays, the hole is significantly (~2 ×) deeper than for the 20 Hz pump experiment. Central lineouts of these plots are shown in Fig. 9(b), where here is plotted the associated refractive index shift Δn. Note that these curves are no longer well fitted by Gaussians at earlier times; thermal diffusion still dominates their evolution, but the interval between thermal source pulses is less than the single pulse dissipation time. Given that the refractive index of undisturbed atmospheric pressure air is $\delta n = n{-}1 \sim 3 \times 10^{-4}$ [14], it is seen that for the conditions of Fig. 9, the index perturbation can be as high as $\Delta n / \delta n \sim 20\%$, a very big effect.
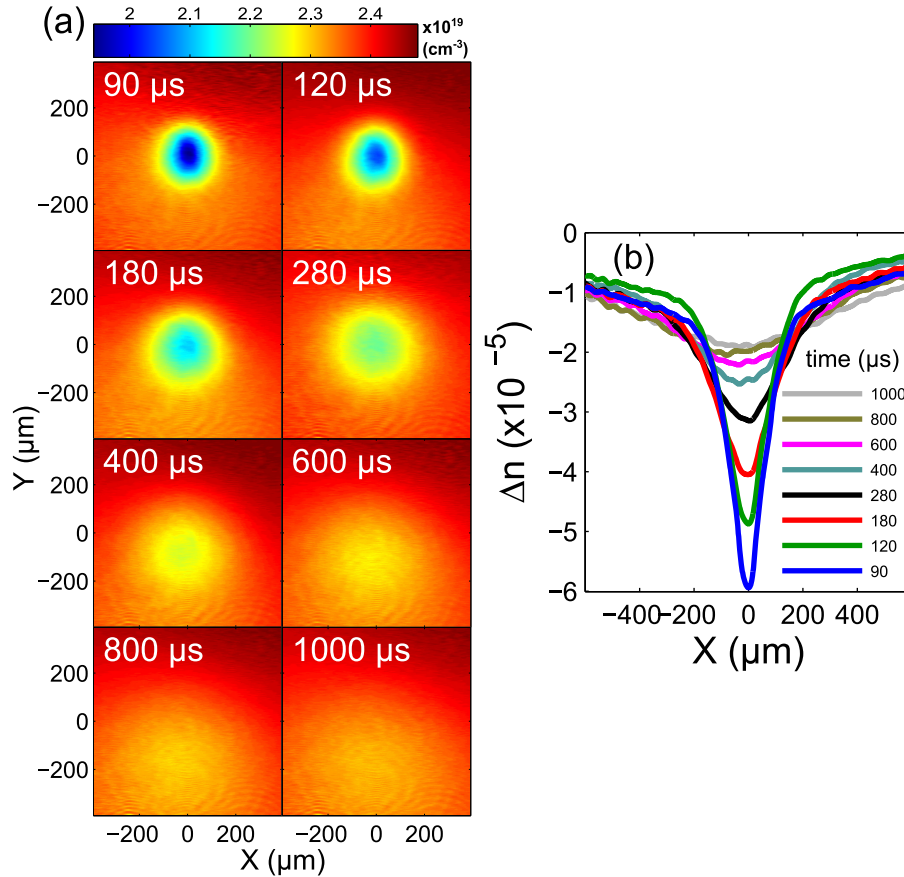

Fig. 9. (a) Density hole profiles in 1 atm air vs. probe delay for pump pulse repetition rate of 1 kHz. (b) Central lineouts of profiles in Fig. 9(a). Here, the associated refractive index shift Δn is shown.

What is the effect of this on laser pulse propagation? In general, the effect of the gas density hole, especially in the highly nonlinear filamentary regime, is best understood with detailed simulations [8], which are now underway. Such simulations will help interpret the details of Figs. 1 and 2. The goal of the present paper, however, is to present measurements of the density hole itself and some demonstrations of its effects on propagation. Below we present qualitative estimates in order to understand the main features of the propagation measurements.

For the case of a 1 kHz pulse train, the defocusing effect of the index hole on the propagating beam can be estimated using the hole refractive index shift Δn sampled across the beam, as seen in Fig. 9(b). The shift ranges from -10^{-6} to -10^{-5}, depending on beam diameter. For higher repetition rates or pump pulse energies, the index shifts would be even

larger. The effective f-number of the density hole which contributes to beam defocusing as strongly as natural beam diffraction is $f_\# = \frac{1}{2}(2\left|\Delta n\right|)^{-1/2}$, giving $f_\#$ ~100 to ~350 for the above range of Δn. Our air filament experiment of Fig. 1 uses f/600 focusing, so it is clear that the cumulative density hole should have a significant defocusing influence. This is seen in Fig. 1, where the entire filament (initial collapse point and later termination) appears to move increasingly downstream from the lens and also lengthens with increasing pulse repetition rate. The increasing repetition rate effect of the long timescale density hole appears to be equivalent to using progressively weaker focusing lenses for filament generation. The supercontinuum generation experiment of Fig. 2 uses f/100 focusing, so the effect of the density hole should also be observable. This is borne out by the significant effect of repetition rate on the spectra, with appreciable blue wings added likely owing to increased filament length.

The mechanism considered thus far for gas density hole generation has been the initial plasma acting as a thermal pressure source. However, another channel for laser energy deposition in gases exists, namely 2-photon Raman excitation of molecular rotation [19]. The excitation manifests itself as an ensemble average molecular alignment with respect to the pump laser polarization. The degree of alignment is expressed as $\left\langle \cos^2\theta \right\rangle_t - \frac{1}{3}$, where $\left\langle \; \right\rangle_t$ refers to a time-dependent average over the molecular ensemble [11] and θ is the angle between the molecular axis and the laser polarization. The average alignment decays due to collisional dephasing over several hundred picoseconds in room temperature, atmospheric pressure gas [11], with the potential energy stored in the alignment being converted to thermal energy. This energy can also be the source for gas density hole generation. In other experiments [11, 12], we have measured maximum alignments $\left(\left\langle \cos^2\theta \right\rangle_t - \frac{1}{3}\right)_{max}$ ~0.05 in nitrogen for laser intensities in the range of 5×10^{13} W/cm^2. The average energy stored per molecule in molecular alignment is roughly estimated as $u_{align} \sim \frac{1}{2}\gamma_{eff}^{max}E^2$, where E is the peak laser electric field and $\gamma_{eff}^{max} = \Delta\alpha\left(\left\langle \cos^2\theta \right\rangle - \frac{1}{3}\right)_{max}$ is the maximum effective molecular polarizability under alignment, where $\Delta\alpha$ is the polarizability anisotropy [11]. For a 100 fs pulse of peak intensity 5×10^{13} W/cm^2 and $\Delta\alpha_{N_2} = 6.7 \times 10^{-25}$ cm^3 [20], we get u_{align}~0.005 eV/molecule. Another estimate is obtained using our density matrix code [21] to calculate the energy invested in the rotational state population transfer excited by the pulse. This gives an average stored energy of 0.004 eV/molecule, in agreement with the alignment-based estimate above.

By comparison, an initial plasma of density N_e~2×10^{16} cm^{-3} and temperature k_BT_e~5 eV generated in atmospheric density N$_2$ repartitions its energy to give ~0.004 eV/molecule. So the effects are of similar size. We are currently investigating this molecular gas heating mechanism and its effect on filamentation in greater detail.